

# Control of the shape and size of iron oxide ($\alpha$-Fe2O3) nanoparticles synthesized through the chemical precipitation method

Abdelmajid Lassoued, Brahim Dkhil, Abdellatif Gadri, Salah Ammar

▶ **To cite this version:**

Abdelmajid Lassoued, Brahim Dkhil, Abdellatif Gadri, Salah Ammar. Control of the shape and size of iron oxide ($\alpha$-Fe2O3) nanoparticles synthesized through the chemical precipitation method. Results in Physics, 2017, 7, pp.3007-3015. 10.1016/j.rinp.2017.07.066 . hal-02317038

**HAL Id: hal-02317038**

**https://centralesupelec.hal.science/hal-02317038**

Submitted on 24 Aug 2020

**HAL** is a multi-disciplinary open access archive for the deposit and dissemination of scientific research documents, whether they are published or not. The documents may come from teaching and research institutions in France or abroad, or from public or private research centers.

L'archive ouverte pluridisciplinaire **HAL**, est destinée au dépôt et à la diffusion de documents scientifiques de niveau recherche, publiés ou non, émanant des établissements d'enseignement et de recherche français ou étrangers, des laboratoires publics ou privés.



Distributed under a Creative Commons Attribution - NonCommercial - NoDerivatives 4.0 International License

Results in Physics 7 (2017) 3007–3015

Contents lists available at ScienceDirect

Results in Physics

journal homepage: www.journals.elsevier.com/results-in-physics

# Control of the shape and size of iron oxide ($\alpha$-$Fe_2O_3$) nanoparticles synthesized through the chemical precipitation method

Abdelmajid Lassoued [a,b,*], Brahim Dkhil [b], Abdellatif Gadri [a], Salah Ammar [a]

[a] Unité de Recherche Electrochimie, Matériaux et Environnement UREME (UR17ES45), Faculté des Sciences de Gabès, Université de Gabès, Cité Erriadh, 6072 Gabès, Tunisia
[b] Laboratory Structures, Properties and Modeling of Solids, Ecole Centrale Paris, CNRS-UMR8580, Grande Voie des Vignes, 92295 Chatenay-Malabry Cedex, France

ARTICLE INFO

*Article history:*
Received 10 July 2017
Accepted 27 July 2017
Available online 1 August 2017

*Keywords:*
Nanoparticles
Hematite ($\alpha$-$Fe_2O_3$)
Precipitation
Precursor
Size
Band gap

ABSTRACT

Hematite ($\alpha$-$Fe_2O_3$) nanoparticles were synthesized via a simple chemical precipitation method. The impact of varying the concentration of precursor on the crystalline phase, size and morphology of $\alpha$-$Fe_2O_3$ products was explored. The characteristic of the synthesized hematite nanoparticles were evaluated by X-ray diffraction (XRD), Transmission Electron Microscopy (TEM), Scanning Electron Microscopy (SEM), Fourier Transform Infra-Red (FT-IR) spectroscopy, Raman spectroscopy, Differential Thermal Analysis (DTA), Thermo Gravimetric Analysis (TGA), Ultraviolet–Visible (UV–Vis) analysis and Photoluminescence (PL). XRD data revealed a rhombohedral (hexagonal) structure with the space group *R*-3*c* in all samples. Uniform spherical like morphology was confirmed by TEM and SEM. The result revealed that the particle sizes were varied between 21 and 82 nm and that the increase in precursor concentration ($FeCl_3$, $6H_2O$) is accompanied by an increase in the particle size of 21 nm for pure $\alpha$-$Fe_2O_3$ synthesized with $[Fe^{3+}] = 0.05$ M at 82 nm for pure $\alpha$-$Fe_2O_3$ synthesized with $[Fe^{3+}] = 0.4$ M. FT-IR confirms the phase purity of the nanoparticles synthesized. The Raman spectroscopy was used not only to prove that we have synthesized pure hematite but also to identify their phonon modes. The thermal behavior of compound was studied by using TGA/DTA results: The TGA showed three mass losses, whereas DTA resulted in three endothermic peaks. Besides, the optical investigation revealed that samples have an optical gap of about 2.1 eV and that this value varies as a function of the precursor concentration.

© 2017 The Authors. Published by Elsevier B.V. This is an open access article under the CC BY-NC-ND license (http://creativecommons.org/licenses/by-nc-nd/4.0/).

## Introduction

The synthesis of hematite particles ($\alpha$-$Fe_2O_3$) of different sizes and shapes was thoroughly examined because their new chemical and physical properties compared to bulk materials, and their potential applications in inorganic pigments [1], catalysts [2], gas and humidity sensors [3,4], photoanode for photo-electrochemical cells [5], photoelectrolysis reactors [6], water treatment [7], and lithium ion batteries [8]. Different techniques have been developed to synthesis hematite particles, such as polyol method [9], sol–gel method [10–12], spray pyrolysis [13–15], hydrothermal technique [16], chemical vapor deposition [17], pulsed laser deposition [18], co-precipitation [19,20] and high vacuum evaporation [19]. In these synthesis methods, size and shape of the compounds change depending on the synthesis parameters, such as the reactant concentration, time and temperature reaction, pH solution, ionic strength, the anions, the surfactant, and the nature of iron salts [21–26]. Moreover, multiple reaction steps are required to obtain the final products. Chemical precipitation method is particularly attractive thanks to its low cost, high purity, short preparation time, high homogeneity, well-crystallized product and relatively low reaction temperature. Liu et al. [27,29] successfully obtained nearly spherical nanoparticles of $\alpha$-$Fe_2O_3$ with a diameter of 60–80 nm.

However, in this work we have attempted to explore the effects of changes in the concentration of precursor used in the synthesis of hematite nanoparticles at the level of size, morphology and optical band gap. We have used precipitation method which stands for a simple procedure to synthesize $\alpha$-$Fe_2O_3$ nanoparticles. The nanoparticles are well characterized for their structural, morphological and optical properties by various characterization techniques such as the X-ray diffraction (XRD), Transmission Electron Microscopy (TEM), Scanning Electron Microscopy (SEM), Fourier Transform Infra-Red (FT-IR) spectroscopy, Raman spectroscopy, Thermo Gravimetric Analysis (TGA), Differential Thermal Analysis (DTA), Ultraviolet–Visible (UV–Vis) analysis and Photoluminescence (PL).

* Corresponding author at: Unité de Recherche Electrochimie, Matériaux et Environnement UREME (UR17ES45), Faculté des Sciences de Gabès, Université de Gabès, Cité Erriadh, 6072 Gabès, Tunisia.
*E-mail address:* abdelmajid.lassoued@yahoo.fr (A. Lassoued).

http://dx.doi.org/10.1016/j.rinp.2017.07.066
2211-3797/© 2017 The Authors. Published by Elsevier B.V.
This is an open access article under the CC BY-NC-ND license (http://creativecommons.org/licenses/by-nc-nd/4.0/).

## Experiments

### Materials

All reagents used in the investigation were analytical grade and used without further purification. Iron(III) chloride hexahydrate ($FeCl_3$, $6H_2O$) (Sigma-Aldrich) was the iron precursor, while ammonia hydroxide ($NH_4OH$) was the precipitating agent, and ethanol ($C_2H_6O$) (Sigma-Aldrich) was used for washing. All solutions were prepared with deoxygenated distilled water.

### Synthesis of hematite nanoparticles

Pure hematite nanoparticles were synthesized with the chemical precipitation method .In this procedure, aqueous solution was prepared by dissolving an amount of iron(III) chloride hexahydrate ($FeCl_3$, $6H_2O$) in 100 mL of deoxygenated distilled water under magnetic stirring for 30 min at 80 °C to obtain a 0.05 M concentration solution (the same principle to obtain solutions of different concentrations (0.1, 0.2 and 0.4 M)). 50 mL aqueous solution of 2 M of $NH_4OH$ was used as the precipitating agent. Base solution ($NH_4OH$) was added gradually drop wise to maintain a pH value of 11. The reaction vessel was heated up to the temperature of 80 °C under magnetic stirring for 3 h. The resulting precipitations were collected and centrifuged at 6000 rpm and then washed with distilled water and ethanol for several times and finally dried in air at 80 °C and calcined at 700 °C for 4 h (Fig. 1).

### Characterization

#### XRD characterizations

The X-ray diffraction patterns of the samples were identified using German Bruker D2 PHASER X-ray diffractometer with $CuK_\alpha$ radiation (1.5418 Å) as a source. The intensity data were collected over the range of 20–80° using a step scan mode (0.001°/s).

#### TEM and SEM measurements

The TEM micrographs were obtained on a JEOL 2011 transmission electron microscope with an accelerating voltage of 200 kV. Micro structural characteristics such as morphology and particle size of samples were analyzed through scanning electron microscope (SEM) with KYKY-EM3200, 25 kV type.

#### Spectroscopy measurements

Fourier Transform Infra-Red (FT-IR) spectra of samples were explored by a NICOLET IR200 FT-IR spectrometer with transmission from 4000 to 400 $cm^{-1}$. The Raman spectra were collected using a Renshaw in Via Raman microscope with a 50× objective coupled to a 632.8 nm He-Ne laser excitation source (Renshaw RL633). The Ultraviolet–Visible (UV–Vis) absorption of the samples was recorded on SHIMADZU (UV-3101 PC) UV–Vis Spectrophotometer. Solid photoluminescence (PL) spectra were taken using a time-resolved Edinburgh Instrument FLSP920 spectrofluorimeter with a Red-PMT detector and a Xenon bulb as an excitation source.

#### Thermal analysis

The thermal behavior was evaluated by Thermo Gravimetric (TGA) and Differential Thermal Analysis (DTA) in the air using TGA Q500 TA instrument.

## Results and discussion

### X-ray diffraction analysis

Fig. 2 shows the X-ray patterns of the samples prepared at 80 °C for 3 h at different concentrations of iron(III) chloride hexahydrate (0.05, 0.1, 0.2 and 0.4 M). All the patterns exhibit the characteristic XRD pattern of hematite (ICDD card no. 33-0664) [29,30]. All the observed peaks can be indexed in agreement with the expected rhombohedral (hexagonal) structure of $\alpha$-$Fe_2O_3$ (space group: *R*-3*c*), with lattice constants of a = 0.5034 nm and c = 1.375 nm [31]. The peaks appearing at 2θ range of 24.16°, 33.12°, 35.63°, 40.64°,

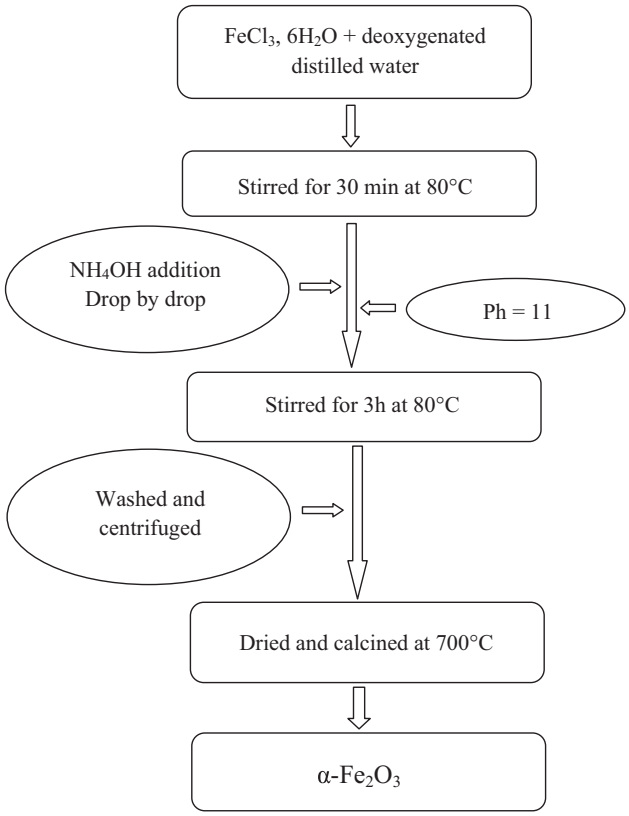



**Fig. 1.** Flowchart for the synthesis of hematite ($\alpha$-$Fe_2O_3$) nanoparticles by precipitation method.

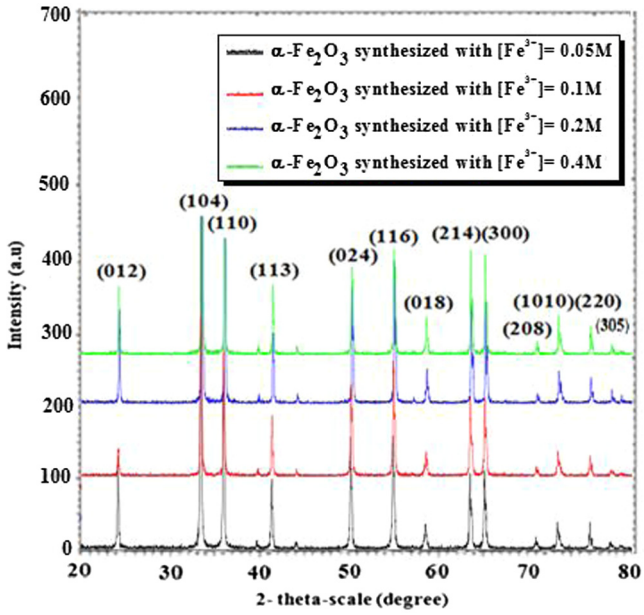



**Fig. 2.** XRD patterns of iron oxide ($\alpha$-$Fe_2O_3$) obtained with chemical precipitation method using different concentrations of precursor.

49.47°, 54.08° and 57.42° can be attributed to the 012, 104, 110, 113, 024, 116 and 018 crystalline structures corresponding to pure α-$Fe_2O_3$ nanoparticles. The narrow sharp peaks indicate that the hematite products are highly crystalline, implying that the high purity of synthesized hematite particles is obtained by using this synthesis method. Moreover, Fig. 2 indicate that when increasing the precursor concentration ($FeCl_3$, $6H_2O$), the intensity of the (1 0 4) diffraction peak decreases gradually and that its half height width is decreased and subsequently the particle size increases.

Given that line broadening of diffraction peaks is affected by the crystallite size and internal strains, the approximate crystallite size "$D_c$" is evaluated using the following Scherer's equation [32].

$$\mathbf{D_c} = \frac{\mathbf{K}\lambda}{\beta \cos\ \theta}$$

where **k** is the so-called shape factor (0.9), λ is the wavelength (0.15418 nm, $CuK_\alpha$), **β** is the full width at half maximum (FWHM), and **θ** is the diffraction angle. The (1 0 4) plane was selected to calculate the crystallite size α-$Fe_2O_3$.

The average crystallite sizes associated with XRD data ranged between 21 and 82 nm. It is thus observed that the size of pure α-$Fe_2O_3$ nanoparticles synthesized with $FeCl_3$, $6H_2O$ increases when the concentration of precursor is increased due to the enhancement in the density of nucleation centers in the synthesized samples.

*Transmission Electron Microscopy (TEM)*

Size and morphology of the nanoparticles are determined by analyzing the recorded TEM images. The TEM images of α-$Fe_2O_3$ nanoparticles obtained from precipitation method and calcined at 700 °C for 4 h are shown in (Fig. 3). After the heat treatment at 700 °C for 4 h, the α-$Fe_2O_3$ particles were found in the range of 21–82 nm. It is clear that hematite nanoparticles are mainly present as granules with small and big spherical shaped particles and are well crystallize in nature. The nanoparticles size depends largely on the concentration of precursor used in the synthesis of hematite. In fact the former varies as we vary the latter. The sizes of nanoparticles were listed in Table 1, which proved that the particle size increased with the raise of the concentration of precursor ($FeCl_3$, $6H_2O$) (Fig. 3) because the reactant with the higher concentration enhanced the merge of crystal nucleus and agglomeration of particles.

**Table 1**
Particle size of different synthesized samples.

| Samples | Particle size (nm) |
|---|---|
| α-$Fe_2O_3$ synthesized with $[Fe^{3+}] = 0.05$ M | 21 |
| α-$Fe_2O_3$ synthesized with $[Fe^{3+}] = 0.1$ M | 39 |
| α-$Fe_2O_3$ synthesized with $[Fe^{3+}] = 0.2$ M | 56 |
| α-$Fe_2O_3$ synthesized with $[Fe^{3+}] = 0.4$ M | 82 |

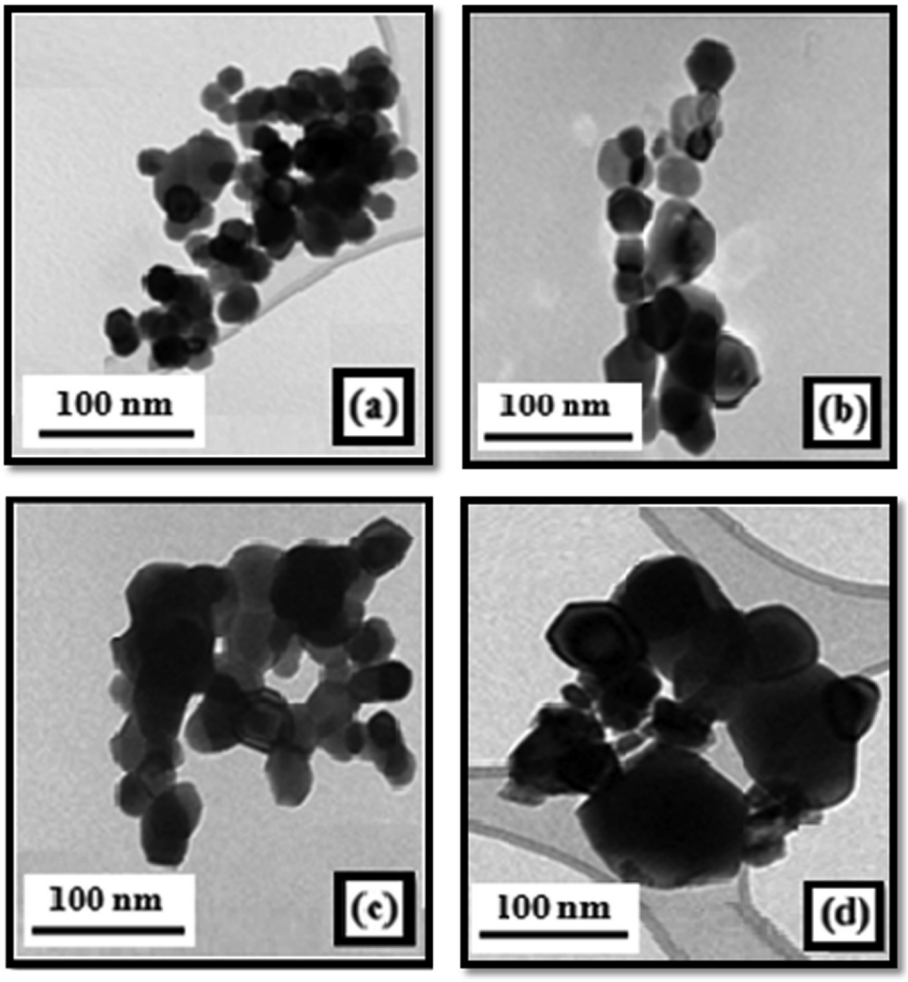



**Fig. 3.** TEM observation of α-$Fe_2O_3$ prepared with different concentrations of $FeCl_3$, $6H_2O$: (a) $[Fe^{3+}] = 0.05$ M, (b) $[Fe^{3+}] = 0.1$ M, (c) $[Fe^{3+}] = 0.2$ M and (d) $[Fe^{3+}] = 0.4$ M.

*Scanning Electron Microscopy (SEM)*

The surface morphologies of the prepared samples were studied using Scanning Electron Microscope. The average sizes of the synthesized hematite nanoparticles under the effects of various preparation conditions are shown in (Fig. 4). All the nanoparticles are spherical in shape. For the effect of the precursor concentration (Fig. 4), the average particle diameter of hematite increases from 21 nm to 82 nm with increasing precursor concentration from 0.05 M to 0.4 M. The reason is that the ($FeCl_3$, $6H_2O$) precursor

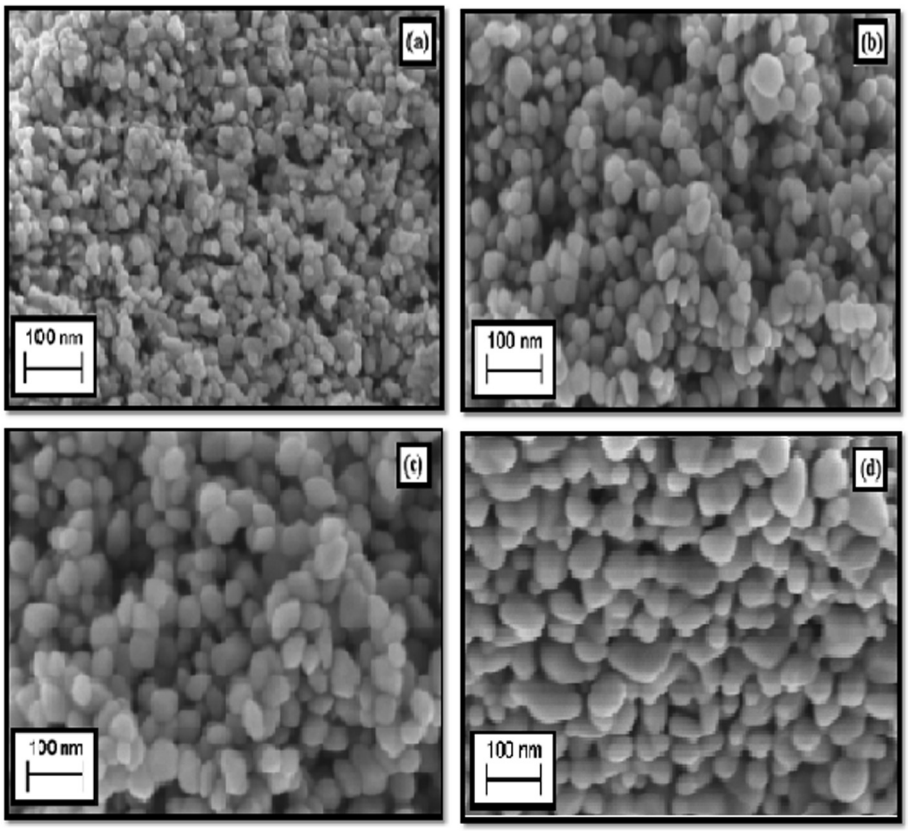



**Fig. 4.** SEM observation of α-$Fe_2O_3$ prepared with different concentrations of $FeCl_3$, $6H_2O$: (a) $[Fe^{3+}]$ = 0.05 M, (b) $[Fe^{3+}]$ = 0.1 M, (c) $[Fe^{3+}]$ = 0.2 M and (d) $[Fe^{3+}]$ = 0.4 M.

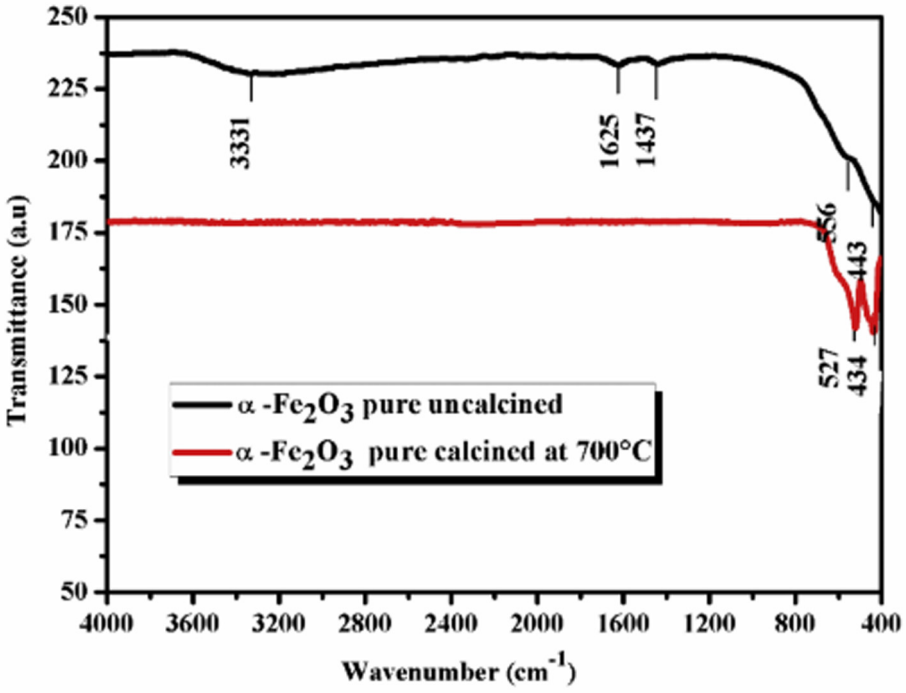



**Fig. 5.** Spectra FT-IR of pure α-$Fe_2O_3$ uncalcined, calcined at 700 °C synthesized by precipitation method.

aggregation creates the nuclei of hematite and the Fe content in this aggregation limits the size of the hematite particles [33]. However, the precursor concentration cannot be further decreased because a low concentration of precursor (e.g., C = 0.05 M) requires longer time to reach the saturation.

*Fourier Transform Infra-Red (FT-IR) spectroscopy*

The formation of nanoparticles was further confirmed by FT-IR spectroscopy. (Fig. 5) shows FT-IR spectra of hematite uncalcined and calcined at 700 °C synthesized with $[Fe^{3+}] = 0.05$ M.

For the uncalcined hematite product, the strong absorption peaks at 556 and 443 $cm^{-1}$ can be attributed to the Fe–O band vibrations [34,35]. The very broad absorption band centered at 3331 $cm^{-1}$ and reaching peak at 1625 $cm^{-1}$ is assigned to the stretching and bending vibrations of the hydroxyl groups and/or water molecules [36], respectively. The findings indicate the presence of not only a small amount of absorbed water on the surface of the product but also structural hydroxyl groups on the same surface as the products were prepared in the aqueous solution. In addition, there is a peak at 1437 $cm^{-1}$ that is assigned to the deformation of $CH_3$.

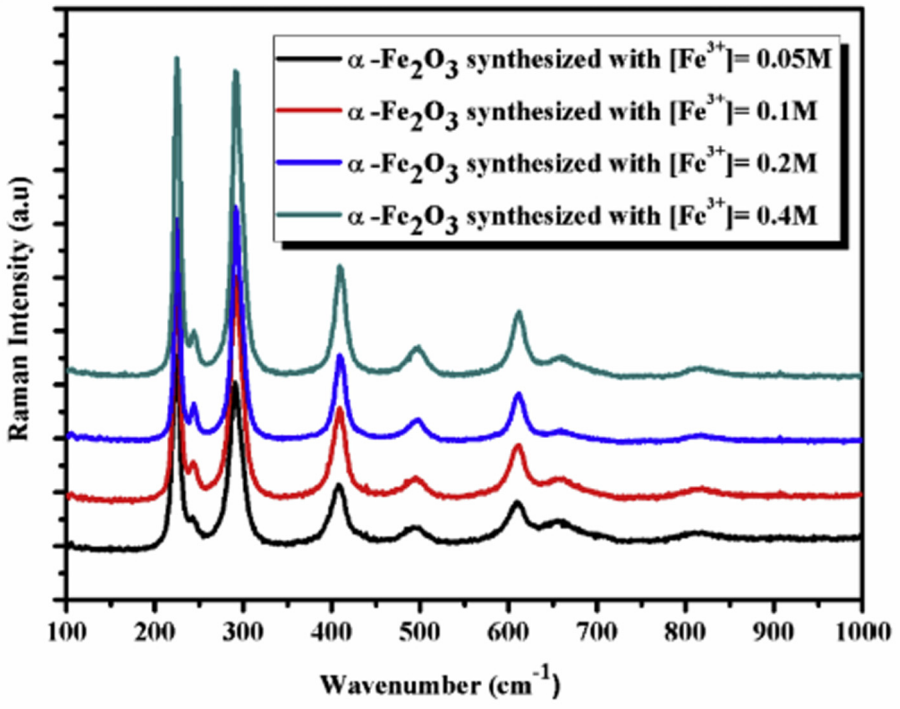



**Fig. 6.** Raman spectra for hematite synthesized with different concentrations of precursor.

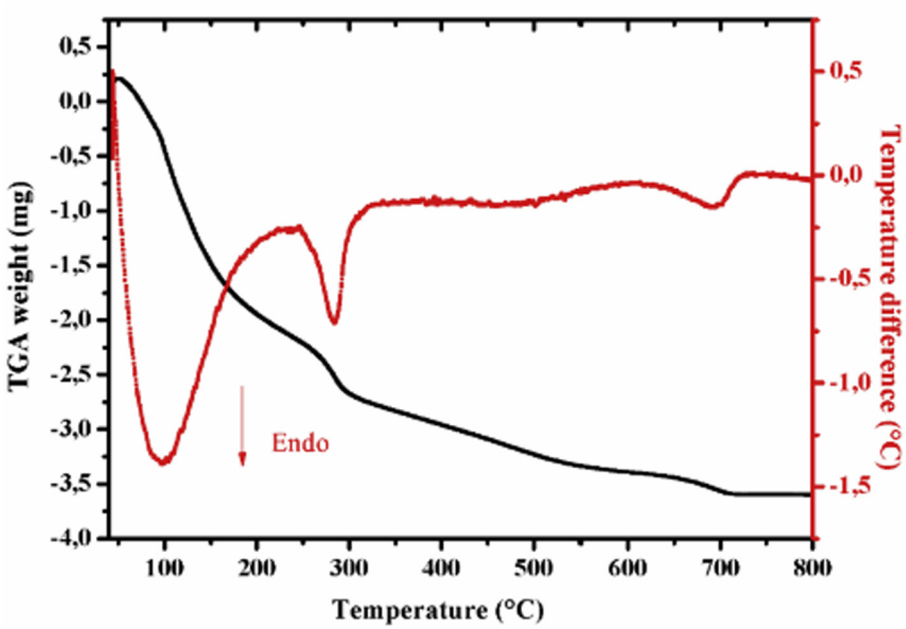



**Fig. 7.** Thermal analyses (TGA, DTA) for pure hematite synthesized with $[Fe^{3+}] = 0.05$ M.

FT-IR spectrum investigations of pure hematite calcined at 700 °C prepared by precipitation method shows the absence of all bands related to the hydroxyl group OH. Yet, all organic species were removed after calcination. Then we noticed the appearance of two bands at 527 and 434 $cm^{-1}$ that can be attributed to the Fe–O vibration in the rhombohedral lattice of hematite [37].

*Raman spectroscopy*

(Fig. 6) portrays the Raman spectra of pure α-$Fe_2O_3$ synthesized with different concentrations of precursor (0.05, 0.1, 0.2 and 0.4) recorded at room temperature using 632.8 nm excitation wavelengths. Pure hematite belongs to the *R*-3*c* crystal space group and seven phonon lines are expected to appear in the Raman spectrum, namely two $A_{1g}$ phonon modes and five $E_g$ phonon modes [38]. The peaks at 227.12 and 494.14 $cm^{-1}$ are associated with the $A_{1g}$ phonon mode while the peaks at 245.73, 292.74, 299, 409.9 and 609.4 $cm^{-1}$ are related to $E_g$ phonon modes. These results prove that the calcined product is α-$Fe_2O_3$. No other iron oxide, such as magnetite or maghemite, was detected, which indicates the high purity of the product. Similar results have been reported with α-$Fe_2O_3$ nanoparticles [39] Indeed, Xu et al. [40] used Raman spectrum to explore the nanoparticles of α-$Fe_2O_3$ synthesized by oxygenating pure iron and identified $A_{1g}$ (225, 498 $cm^{-1}$), $E_g$ (252, 293, 411, 612 $cm^{-1}$).

The Raman spectrum of hematite synthesized with $[Fe^{3+}]$ = 0.05 M is identical to the Raman spectra of α-$Fe_2O_3$ synthesized with the other precursor concentrations (0.1, 0.2 and 0.4).

*Thermal study*

The findings associated with formation and decomposition phase occurring during heat treatment of synthesized samples are in good agreement with Thermo Gravimetric Analysis and Differential Thermal Analysis (TGA and DTA) results. Thermal analyses were carried out from room temperature to 700 °C. TGA of the prepared compound was performed by heating the samples in air atmosphere at 10 °C/min in alumina crucible. (Fig. 7) depicts the thermal analyses (TGA, DTA) for pure hematite synthesized with $[Fe^{3+}]$ = 0.05 M.

As for α-$Fe_2O_3$ prepared by precipitation method (Fig. 7), there are three distinct mass loss steps in the temperature ranges. The first weight loss step occurred gradually between [44–182 °C]. The mass loss was of 5.56%, and this loss of weight is attributed to the removal of water existing on the surface of α-$Fe_2O_3$. Using DTA enabled us to find one endothermic peak at 99.82 °C, The second step corresponds to a mass loss of 3.04% occurring at [182–540 °C], which is due to the combustible organic products present in our prepared sample. Through the use of DTA we recorded one endothermic peak at 186.28 °C. The third step stands for a minor weight loss (1.38%) occurring in the range of [540–660 °C], which is due to the transition phase of synthesized compounds. Finally using DTA helped us find one endothermic peak at 656.02 °C. After 660 °C, the curve becomes parallel to the temperature axis, which emphasizes high stability of α-$Fe_2O_3$ nanoparticles. There is no associated signal with the thermal processes of α-$Fe_2O_3$ nanoparticles in the TGA curve confirming the crystallization and phase transition of α-$Fe_2O_3$ nanoparticles associated with them.

*UV–Visible analysis*

The absorption spectra in the UV–Vis range of hematite synthesized with different concentrations of precursor show that all absorption curves exhibit an intense absorption in the range of 500–700 nm wavelength (Fig. 8). This result is consistent with data from other studies [40–42]. The optical band gap ($E_g$) for hematite nanoparticles can be determined by extrapolation from the absorption edge which is given by the following equation [43]:

$$(\boldsymbol{\alpha h\nu})^{\mathbf{n}} = \mathbf{A}\ (\mathbf{h\nu} - \mathbf{E_g})$$

where **α** is the absorption coefficient, **A** is constant, **hν** is the energy of light and **n** is a constant depending on the nature of the electron transition [44]. Hematite has a direct band gap (n = 2) [45]. (Fig. 9)

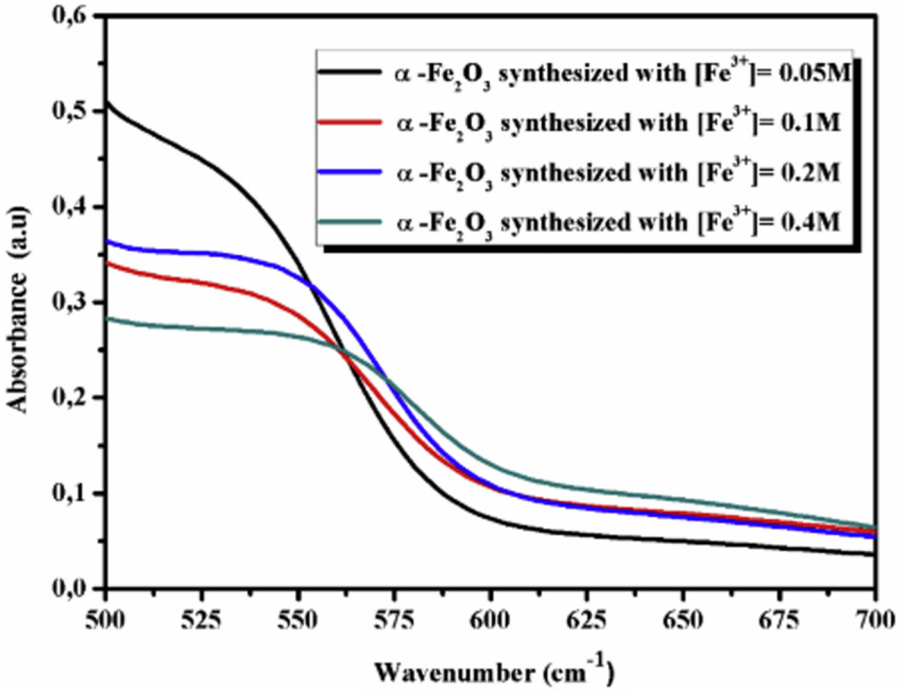



**Fig. 8.** UV–Vis DRS spectra of α-$Fe_2O_3$ obtained through the chemical precipitation method with different concentrations of precursor.

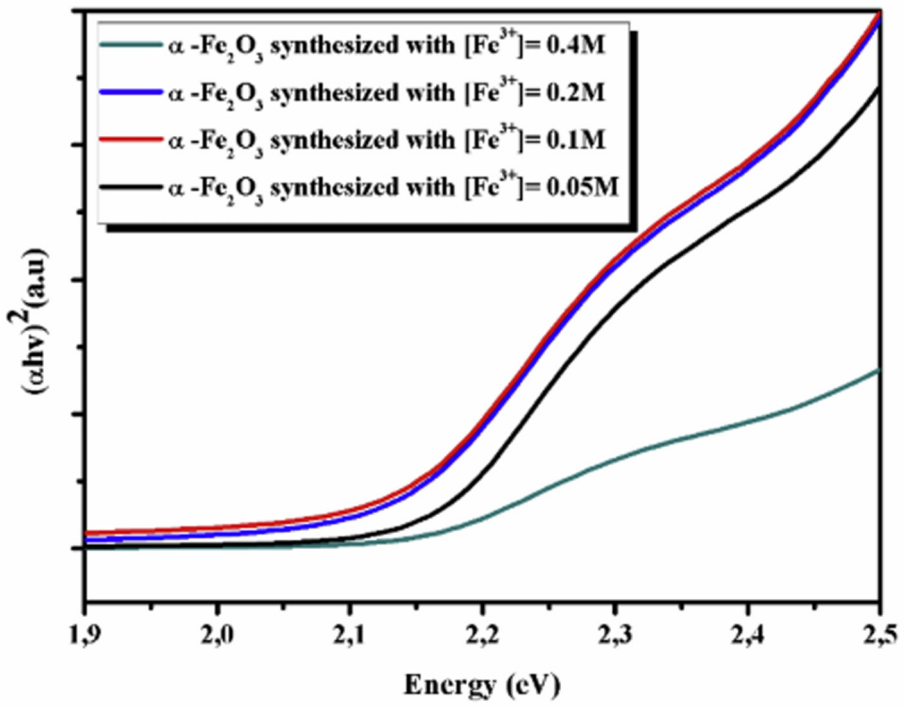



**Fig. 9.** Tauc plot obtained with UV–Vis DRS spectra of $\alpha$-$Fe_2O_3$ resulting from the chemical precipitation method using different concentrations of precursor.

shows the plot of $(\alpha h\nu)^2$ versus $h\nu$. The energy gap can be obtained from the intercept of the linear absorption edge part with the energy axis. When $(\alpha h\nu)^2$ is zero, the photon energy is $E_g$. The decrease in the particle size of hematite synthesized with different concentrations of precursor is responsible for increasing the optical band gap of 1.96–2.09 eV where, the relation between them is inverse relationship.

*Photoluminescence*

Taking into account the excellent luminescent properties of $d^6$ metal complexes and to explore the potential application as luminescent materials, solid-state fluorescent properties of the title compound was studied. The PL spectrum of the sample at room temperature excited at 250 nm is depicted in (Fig. 10). This

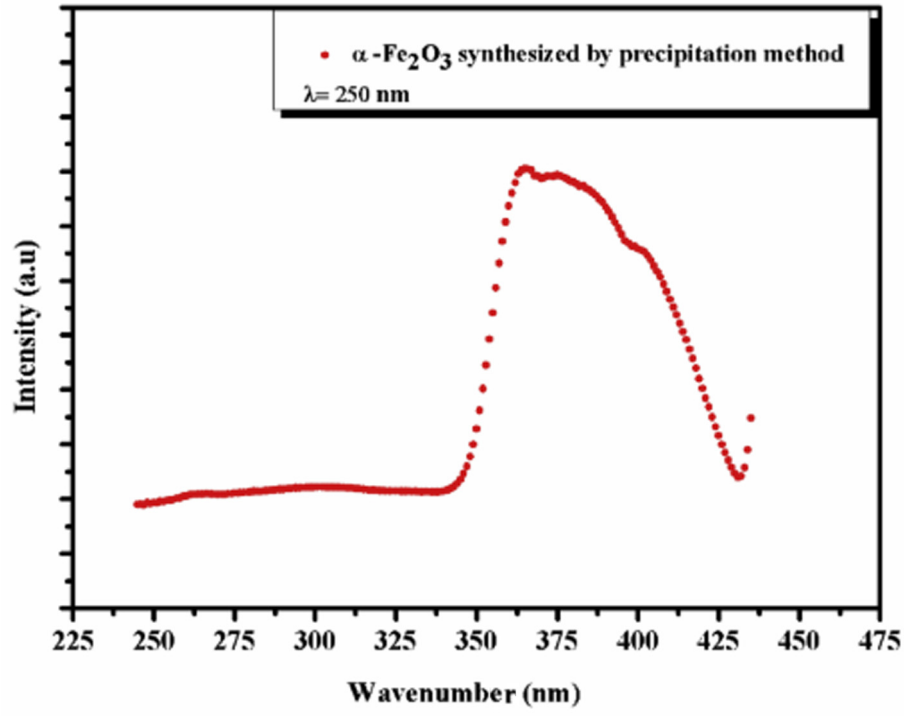



**Fig. 10.** Excitation fluorescence profile of hematite synthesized with $[Fe^{3+}] = 0.05$ M.

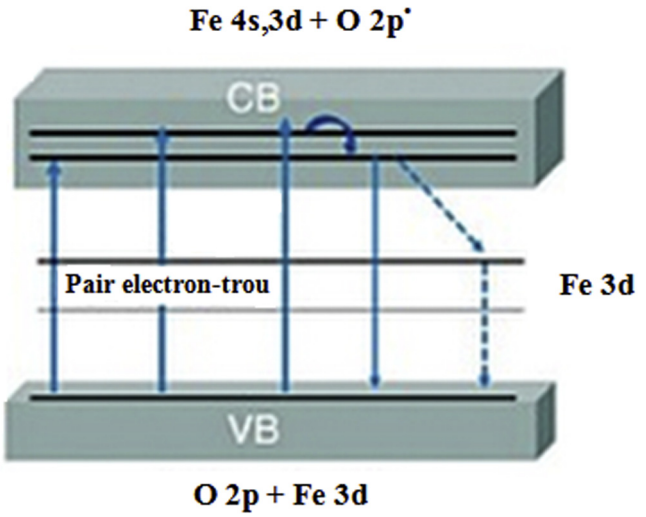



**Fig. 11.** Simple model for the formation and recombination of the exciton in the title compound.

material shows one band of luminescence located at 370 nm (3.35 eV), this luminescence can be observed even with the naked eye at room temperature and is due to exciton emission [46]. The luminescence originates from electronic transition within the iron oxide ($\alpha$-$Fe_2O_3$). In this compound, the lowest exciton state arises from excitation between the Valence Band (VB), which consists of a mixture of Fe (3d) and O (2p) states, and the Conduction Band (CB) which derives primarily from Fe (4s) states. Under excitation of 363 nm irradiation, an electron (−) is excited from the VB to the CB, leaving a hole (+) in the VB. The exciton (−) and the hole (+) move freely in the CB and VB, forming an exciton, the recombination of the electron and hole in the exciton yields a red emission at 370 nm (Fig. 11).

## Conclusion

In this study, hematite nanoparticles were prepared by precipitation method with different concentrations of precursor (0.05, 0.1, 0.2 and 0.4 M). The effects of changes in the concentration of precursor used in the synthesis of $\alpha$-$Fe_2O_3$ nanoparticles at the level of size, morphology and optical band gap were explored. XRD, TEM, SEM, FT-IR, Raman spectroscopy, DTA, TGA, UV–Vis and PL techniques were used to characterize the synthesized samples. The results of the different techniques show that the increase of the precursor concentration leads to an increase of size of nanoparticles. In conclusion, the lowest concentration of $FeCl_3$, $6H_2O$ ($[Fe^{3+}] = 0.05$ M) resulted in the smallest size (21 nm) and best crystallinity of hematite nanoparticles. Moreover, hematite synthesized with $[Fe^{3+}] = 0.05$ M yielded the biggest band gap ($E_g = 2.09$ eV). Future work will investigate the photocatalytic application of $\alpha$-$Fe_2O_3$ compound in effluent water treatment.

## Acknowledgments

The present work was supported by the Research Funds of Electrochemistry, Materials and Environment Research Unit UREME (UR17ES45), Faculty of Sciences Gabes University, Tunisia and Structures, Properties and Modeling of Solids (SPMS) Laboratory, Ecole Centrale Paris, France.

## References

[1] Hosseini-Zori M, Bondioli F, Manfredini T, Taheri-Nassaj E. Effect of synthesis parameters on a hematite-silica red pigment obtained using a coprecipitation route. Dyes Pigment 2008;77:53–8.
[2] Brown ASC, Hargreaves JSJ, Rijniersce B. A study of the structural and catalytic effects of sulfation on iron oxide catalysts prepared from goethite and ferrihydrite precursors for methane oxidation. Catal Lett 1998;53:7–13.
[3] Chauhan P, Annapoomi S, Trikha SK. Humidity-sensing properties of nanocrystalline haematite thin films prepared by sol–gel processing. Thin Solid Films 1999;346:266–8.
[4] Huo L, Li W, Lu L, Cui H, Xi S, Wang J, et al. Preparation structure and properties of three-dimensional ordered $\alpha$-$Fe_2O_3$ nanoparticulatefilm. Chem Mater 2000;12:790–4.
[5] Watanabe A, Kozuka H. Photoanodic properties of sol–gel-derived Fe thin films containing dispersed gold and silver particles. J Phys Chem B 2003;107:12713–20.
[6] Kay A, Cesar I, Gratzel M. New benchmark for water photo-oxidation by nanostructured $\alpha$-$Fe_2O_3$ films. J Am Chem Soc 2006;128:15714–21.
[7] Cao S, Zhu Y. Hierarchically nanostructured $\alpha$-$Fe_2O_3$ hollow spheres: preparation, growth mechanism, photocatalytic property, and application in water treatment. J Phys Chem C 2008;112:6253–7.
[8] Wu Z, Yu K, Zhang S, Xie Y. Hematite hollow spheres with a mesoporous shell. controlled synthesis and applications in gas sensor and lithium ion batteries. J Phys Chem C 2008;112:11307–13.
[9] Jung DW, Park DW. Synthesis of nano-sized antimony-doped tin oxide (ATO) particles using a DC arc plasma jet. Appl Surf Sci 2009;255:5409–13.
[10] Bernardi MIB, Cava S, Paiva-Santos CO, Leite ER, Paskocimas CA, Longo E. Comparison of blue pigments prepared by two different methods. J Eur Ceram Soc 2002;22:2911–9.
[11] Lan F, Wang X, Xu X. Preparation and characterization of SnO2 catalysts for. CO and CH4 oxidation. React Kinet Mech Catal 2012;106:113.
[12] Morazzoni F, Canevali C, Chiodini N, Mari C, Ruffo R, Scotti R, et al. Surface reactivity of nanostructured tin oxide and Pt-doped tin oxide as studied by EPR and XPS spectroscopies. Mater Sci Eng 2001;15:167–9.
[13] Zhang J, Colbow K. Silver diffusion and pattern formation on polycrystalline tin oxide films. J Appl Phys 1992;71:2238–42.
[14] Messad A, Bruneaux J, Cachet H, Froment M. Analysis of the effects of substrate temperature, concentration of tin chloride and nature of dopants on the structural and electrical properties of sprayed SnO2 films. J Mater Sci 1994;29:5095–103.
[15] Kim H, Pique A. Transparent conducting Sb-doped SnO2 thin films grown by pulsed-laser deposition. Appl Phys Lett 2004;84:218–20.
[16] Zhang JR, Gao L. Synthesis and characterization of antimony-doped tin oxide (ATO) nanoparticles by a new hydrothermal method. Mater Chem Phys 2004;87:10–3.
[17] Kim KS, Yoon SY, Lee WJ, Kim KH. Surface morphologies and electrical properties of antimony-doped tin oxide films deposited by plasma-enhanced chemical vapor deposition. Surf Coat Technol 2001;138:229–36.
[18] Thai TMN, Kim SR, Kim HJ. Synthesis of Fe2O3 polymorph thin films via a pulsed laser deposition technique. New Phys Sae Mulli 2014;64:252–5.
[19] Rinnert H, Miska P, Vergnat M, Schmerber G, Colis S, Dinia A, et al. Photoluminescence of Nd-doped SnO2 thin films. Appl Phys Lett 2012;100. 101908(1)–101908(3).
[20] Tian ZM, Yuan SL, He JH, Li P, Zhang SQ, Wang CH, et al. Structure and magnetic properties in Mn doped SnO2 nanoparticles synthesized by chemical co-precipitation method. J Alloys Compd 2008;466:26–30.
[21] Cornell RM, Giovanoli R. Effect of solution conditions on the proportion and morphology of goethite formed from ferrihydrite. Clays Clay Miner 1985;33:424–32.
[22] Schwertmann U, Friedl J, Stanjek H. From Fe (III) ions to ferrihydrite and then to hematite. J Colloid Interface Sci 1999;209:215–23.
[23] Kandori K, Ohnishi S, Fukusumi M, Morisada Y. Effects of anions on the morphology and structure of hematite particles produced from forced hydrolysis of Fe(NO3)3–HNO3. Colloids Surf 2008;331:232–8.
[24] Nyirő-Kósa I, Rečnik A, Pósfai M. Novel methods for the synthesis of magnetite nanoparticles with special morphologies and textured assemblages. J Nanoparticle Res 2012;14:1150–9.
[25] Ming M, Yu Z, Zhirui G, Ning G. Facile synthesis of ultrathin magnetic iron oxide nanoplates by Schikorr reaction. Nanoscale Res Lett 2013;8:16–22.
[26] Ibrahim A, Abubakar AB. Some wet routes for synthesis of hematite nanostructures. Afr J Pure Appl Chem 2013;7:114–21.
[27] Liu H, Guo H, Li P, Wei Y. The transformation of ferrihydrite in the presence of trace Fe (II): the effect of the anionic media. J Solid State Chem 2008;181:2666–71.
[28] Liu H, Wei Y, Sun Y. The formation of hematite from ferrihydrite using Fe (II) as a catalyst. J Mol Catal A Chem 2005;226:135–40.
[29] Hua J, Gengsheng J. Hydrothermal synthesis and characterization of. monodisperse $\alpha$-$Fe_2O_3$ nanoparticles. Mater Lett 2009;63:2725–7.
[30] Almeida T, Fay M, Zhu YQ, Brown PD. Process map for the hydrothermal synthesis of $\alpha$-$Fe_2O_3$ nanorods. J Phys Chem C 2009;113:18689–98.
[31] Teja AS, Koh PY. Synthesis, properties, and applications of magnetic iron oxide nanoparticles. Prog Cryst Growth 2009;55:22–45.
[32] Klug P, Alexander LE, X-ray diffraction procedures: for polycrystalline and amorphous materials, vol. 32, Wiley; 1974. p. 992–9.

[33] Lassoued A, Lassoued MS, Dkhil B, Gadri A, Ammar S. Structural, optical and morphological characterization of Cu-doped α-$Fe_2O_3$ nanoparticles synthesized through co-precipitation technique. J Mol Struct 2017;1148:276–81.
[34] Liu H, Li P, Lu B, Wei Y, Sun Y. Transformation of ferrihydrite in the presence or absence of trace Fe(II): the effect of preparation procedures of ferrihydrite. J Solid State Chem 2009;182(1767–17):71.
[35] Jing Z, Wu S. Synthesis and characterization of monodisperse hematite nanoparticles modified by surfactants via hydrothermal approach. Mater Lett 2004;58:3637–40.
[36] Darezereshki E. One-step synthesis of hematite (α-$Fe_2O_3$) nano-particles by direct thermal-decomposition of maghemite. Mater Lett. 2011;65:642–5.
[37] Cornell RM, Schwertmann U. Electronic, electrical and magnetic properties and colour, the iron oxides. Darmstadt: Wiley-VCH Verlag GmbH & Co. KGaA; 2004. p. 111–37.
[38] de Faria DLA, Venâncio Silva S, de Oliveira MT. Raman microspectroscopy of some iron oxides and oxyhydroxides. J Raman Spectrosc 1997;28:873–8.
[39] Bersani D, Lottici P, Montenero A. Raman scattering characterization of gel-derived titania glass. J Raman Spectrosc 1999;30:355–60.
[40] Xu YY, Zhao D, Zhang XJ, Jin WT, Kashkarov P, Zhang H. Synthesis and characterization of single-crystalline α-$Fe_2O_3$ nanoleaves. Phys E 2009;41:806–11.
[41] Sivakumar S, Anusuya D, Khatiwada CP, Sivasubramanian J, Venkatesan A, Soundhirarajan P. Characterizations of diverse mole of pure and Ni-doped α-$Fe_2O_3$ synthesized nanoparticles through chemical precipitation route. Spectrochim Acta A 2014;128:69–75.
[42] Bagheri S, Chandrappa KG, Bee Abd Hamid S. Generation of hematite nanoparticles via sol-gel method. Res J Chem Sci 2013;3:62–8.
[43] Shen S, Kronawitter CX, Jiang J, Mao SS, Guo L. Surface tuning for promoted charge transfer in hematite nanorod arrays as water-splitting photoanodes. Nano Res 2012;5:327–36.
[44] Branek R, Kisch H. Tuning the optical and photoelectrochemical properties of surface-modified TiO2. Photochem Photobiol Sci 2008;7:40–8.
[45] Pankove JI. Optical processes in semiconductors. Englewood Cliff, New Jersey: Prentice-Hall Inc.; 1971. p. 34–86.
[46] Ling Y, Wheeler DA, Zhang JZ, Li Y. Optical properties and applications of hematite (α-$Fe_2O_3$) nanostructures. One-Dimensional Nanostructures: Principles and Applications, 2013. p. 167–84.